



Research paper

A potential descriptor for the CO₂ hydrogenation to CH₄ over Al₂O₃ supported Ni and Ni-based alloy catalysts

Koustuv Ray, Goutam Deo *

Department of Chemical Engineering, Indian Institute of Technology, Kanpur, 208 016, India

ARTICLE INFO

Article history:

Received 29 March 2017

Received in revised form 28 June 2017

Accepted 4 July 2017

Available online 5 July 2017

Keywords:

Ni-Fe and Ni-Cu alloy

CO₂ methanation

d-density of states (d-DOS)

Descriptor

ABSTRACT

Supported Ni, Cu, Fe, and Ni-M (M = Cu or Fe) catalysts of the same total metal loading and different Ni to M ratios are examined for the CO₂ hydrogenation to CH₄. Substituting Ni with Cu or Fe in a Ni/Al₂O₃ catalyst leads to smaller average particle size, sharper particle size distribution and alloy formation, which were determined from transmission electron microscopy (TEM) and X-ray diffraction (XRD). Surface properties of the Ni/Al₂O₃ and Ni-M/Al₂O₃ catalysts are found to be different as revealed by hydrogen temperature programmed desorption (H₂-TPD). Furthermore, the surface of the supported Ni-Cu catalyst was enriched with Cu. The catalytic activity increases for 75Ni25Fe/Al₂O₃ relative to Ni/Al₂O₃, but decreases for 75Ni25Cu/Al₂O₃. In both these catalysts, the Ni to M ratio was 3:1. The supported Ni and the two Ni₃M alloy catalysts are modelled successfully as the shift in θ between experimental and simulated XRD pattern were in accordance. Moreover, the trend in shifts in experimental and simulated optimized lattice constants relative to Ni was similar. Density functional theory (DFT) calculations revealed changes in the electronic properties. The electronic properties calculated based on the d-density of states (d-DOS) of surface Ni atoms are the d-band center (ε_d) and number of d-DOS at Fermi level (N_{E_F}). An excellent correlation between TOF_{CH₄} and N_{E_F} exists, whereas ε_d did not satisfactorily capture the trends in TOF_{CH₄}. Thus, the N_{E_F} best describes the catalytic activity trend of the supported Ni and two Ni-based alloy catalysts.

© 2017 Elsevier B.V. All rights reserved.

1. Introduction

Extensive use of fossil fuels as the primary source of energy to meet the energy demand increases the concentration of greenhouse gases (GHGs) in the atmosphere. This poses a severe threat to civilization due to global-warming induced climate change and ocean acidifications. More than 80% of total GHGs consist of CO₂. Thus, mitigation of CO₂ is of utmost importance for sustainable development. Moreover, considering the rising population and increasing energy demands, where dependence on fossil fuels is not expected to decline soon, chemical conversion of CO₂ to useful products is a more attractive and promising solution than capturing and geologically sequestering CO₂. Similar to conventional syngas based Fischer-Tropsch synthesis technology; CO₂ hydrogenation can also produce a wide range of chemicals that include hydrocarbon, higher alcohol and liquid fuels [1–6]. Currently, there is an increasing trend in utilizing CO₂ to produce a variety of value added products. These products are used as fuels or chemicals and/or are further processed to produce more complex products [1–4,6–8].

The CO₂ hydrogenation to CH₄ is one such process where CO₂ is converted to a value added product. This catalytic conversion of CO₂ can in some way assist in combating climate change, ocean acidification and associated greenhouse gas emission by recycling atmospheric carbon, which is a crucial element in human life and civilization. The CO₂ hydrogenation to methane is also known as the Sabatier reaction. Although it is a very old reaction, CO₂ methanation still finds relevance for the large-scale manufacture of substitute natural gas from the products of coal gasification, removal of trace CO from H₂ rich streams for use in fuel cell and ammonia synthesis. Recently, NASA has also shown the use of this reaction for future manned space colonization on Mars [7]. Moreover, this reaction has been considered as a probe reaction for understanding catalytic system of interests and deriving mechanistic insights [9–15]. Therefore, CO₂ methanation is an important catalytic process of fundamental academic interest with viable commercial application.

Catalytic CO₂ hydrogenation to methane has been studied over supported transition metal catalysts including Ni, Rh, Ru, Co, Pt, Au, Cu [1–5,7,8,16,17]. Ni/Al₂O₃ is an existing CO methanation catalyst that is industrially used [18,19]. Small amounts of CO₂ are also present in the reactant stream. Several supports, including CeO₂, ZrO₂, TiO₂, Al₂O₃ and SiO₂, have been used to test the activity of

* Corresponding author.

E-mail address: goutam@iitk.ac.in (G. Deo).

metal catalysts for this reaction [1,4,7,8]. Although Ni on basic support, such as $\text{CeO}_2\text{-ZrO}_2$ mixed oxide, showed promising results, significant testing and fundamental research has taken place on $\text{Ni/Al}_2\text{O}_3$ catalysts [7,20–22]. The $\text{Ni/Al}_2\text{O}_3$ is a much investigated catalyst for the methanation reaction and the catalytic activity was found to depend on Ni metal loading [21,22]. It was confirmed that methane production rate per unit Ni surface area was the highest for 5 wt.% NiAl_2O_3 among the series of $\text{Ni/Al}_2\text{O}_3$ catalysts with loading ranging from 5 wt.% to 25 wt.% [22]. The low sized (10–30 nm) metallic Ni is responsible for maximum selectivity towards CH_4 without any gas phase CO being formed [21]. Moreover, this reaction depends on the oxidation state of Ni species [21]. Partly oxidized Ni caused lowering in methanation activity under dynamic reaction condition as shown by Grunwaldt et al. [20]. Noble metals including Rh, Ru are more active than Ni. However, the high cost of noble metal based catalysts has restricted their use. Bimetallic catalysts with Ni as the primary metal have shown superior catalytic activity compared to Ni for the CO_2 methanation reaction [11]. Unlike conventional methanation catalyst, where CO is the primary component in the feed, catalysts for CO_2 methanation require more exploration. Among the few studies on Ni based bimetallic catalysts, the higher activity for CH_4 formation relative to Ni has been ascribed to alloy formation [11,23]. A previous study has shown that in comparison with commonly used supports the Al_2O_3 supported Ni-Fe bimetallic catalyst performs best for CO_2 methanation [24]. Ni-Cu bimetallic catalyst has also been investigated for a number of reactions including methanation, higher alcohol synthesis, dehydrogenation, methanol synthesis and water gas shift reactions [25,26].

The enhanced activity by the bimetallic/alloy catalysts over their monometallic counterpart was argued to occur due to of synergy between the two metals [1,2,7]. This synergy alters the structural and electronic property of the primarily active metal, and changes in the binding energy of the reactants and key intermediates are formed. These alterations bring about overall changes in the activation energy of the rate determining step favouring improved catalytic activity. The key factors of the alloy catalysts that improve the catalytic activity need to be understood in terms of these governing factors. These key factors, coined as descriptors, form the milestone in heterogeneous catalytic reactions. The descriptors influence the mechanistic steps and contribute to the fundamental changes in mechanistic pathways. Descriptor based catalyst design has gained significant attention owing to the theory of Hammer and Norskov [27–31]. Electronic and geometric factors play a pivotal role in establishing the descriptors [28,29,31]. A suitable descriptor needs to address not only the improved activity for certain bimetallic catalysts, but also the decrease in activity of other systems. The d-band center, ε_d , is one of the descriptors, which correlate with the surface reactivity for a number of reactions [2,32–35]. Despite the advancement, suitable descriptors for the CO_2 methanation over Ni based bimetallic/alloy catalysts are still lacking.

Our current research attempts to find a suitable descriptor for CO_2 methanation that is valid for Al_2O_3 supported Ni, Ni-Fe and Ni-Cu catalysts of specific compositions. Specifically, the effect of substituting Ni with Cu or Fe on the catalytic properties and activities of Al_2O_3 supported Ni system is examined. All the catalysts were synthesized and characterized by H_2 -temperature programmed reduction ($\text{H}_2\text{-TPR}$), X-ray diffraction (XRD), H_2 -temperature programmed desorption ($\text{H}_2\text{-TPD}$) techniques, X-ray photoelectron spectroscopy (XPS) and finally tested for the CO_2 methanation reaction. Transmission electron microscopy (TEM) was also carried out on Al_2O_3 supported Ni and Ni-M catalysts of specific compositions to obtain particle size distribution and the average particle size was determined. Finally, correlations are achieved by combining the results of catalytic activity measurements with combined characterization information and DFT

calculations in order to suggest a potential descriptor for the CO_2 methanation reaction being carried out with Ni and Ni-M bimetallic catalysts.

2. Experimental

2.1. Catalyst Synthesis

Three monometallic (Ni, Cu, Fe) and two series of bimetallic (Ni-Cu, Ni-Fe) supported catalysts were prepared by the incipient wetness impregnation (IWI) over commercially available $\gamma\text{-Al}_2\text{O}_3$ (SASOL) support. A total metal loading of 15 wt.% was attempted for each supported catalyst. The maximum total metal loading was constrained since a single IWI allowed a maximum metal loading of 15 wt.%. The Al_2O_3 support was initially impregnated with an incipient wetness volume of water. The incipient wetness volume was estimated by taking 1 g of the Al_2O_3 support in a small glass beaker and adding double distilled water drop-wise with simultaneous mixing until a homogeneous paste was formed. Precursor solutions were made by dissolving required quantity of $\text{Ni}(\text{NO}_3)_2\cdot 6\text{H}_2\text{O}$ (Sigma-Aldrich, 99.99%), $\text{Cu}(\text{NO}_3)_2\cdot 3\text{H}_2\text{O}$ (Sigma-Aldrich, 99%) and/or $\text{Fe}(\text{NO}_3)_3\cdot 9\text{H}_2\text{O}$ (Sigma-Aldrich, 99.99%) in an known amount of distilled water that was sufficient to fill the pores of the support. The precursor solution was added drop-wise to the pretreated support and the mixture was intermittently stirred during the process of adding the precursor solution. The resulting mixture was then dried and calcined at increasing temperatures and finally at 773 K for 6 h. The calcined catalysts were then reduced in a reactor at 823 K for 4 h under flowing H_2 stream to achieve supported monometallic and bimetallic catalysts. The sample nomenclature and nominal compositions are given in Table 1.

2.2. Catalyst characterization

2.2.1. Metal composition and surface area

The metal composition of the synthesized catalysts was obtained from a Rigaku ZSX Primus II spectrophotometer. Rhodium (Rh) tube was taken as the source of radiation.

The specific surface area of the calcined catalysts was measured by N_2 physisorption at 77 K using an Autisorb-iQ (Quantachrome). The BET surface area was determined using a 7-point linear plot with partial pressure ratios ranging from 0.05 to 0.3. All the samples were degassed at 498 K for 8 h prior to surface area measurements.

2.2.2. X-ray diffraction (XRD)

X-ray diffraction patterns of the calcined and reduced catalysts were collected on an X'Pert PRO Diffractometer (PANalytical) that used Ni filtered $\text{Cu-K}\alpha$ radiation and operated at 45 kV and 40 mA. The patterns were recorded in the 2θ range from 30° to 80° . A sweep of 3° min^{-1} and a time constant of 3 s were employed. The crystalline phases were analyzed by the Pearson's Crystal Data (PCD) library. The crystallite size of some of the reduced catalysts was calculated by using the highest intensity peak of the metal and/or alloy. To obtain the XRD patterns of the reduced samples, the calcined samples were reduced *ex situ* in a down flow tubular quartz reactor under a flow of H_2 (30 ml/min at STP) at 823 K for 4 h prior to the measurement.

2.2.3. Hydrogen-temperature programmed reduction ($\text{H}_2\text{-TPR}$)

The reducibility of the calcined catalysts was examined by $\text{H}_2\text{-TPR}$ using an Altamira AMI-200 instrument, which was equipped with a thermal conductivity detector (TCD). In these experiments, 50 mg of calcined sample was placed in a U-shaped quartz reactor and heated up to 623 K at 10 K/min under a flow of Argon (Ar) (30 ml/min at STP) and held at this temperature for 1 h. The reactor

Table 1

Sample nomenclature and characterization information of 15Ni/Al₂O₃, Ni-M/Al₂O₃ and 15 M/Al₂O₃ catalysts. M = Cu or Fe. Samples were reduced at 823 K for 4 h prior to analysis.

Sample nomenclature	% Metal loading (g metal/g catalyst)		Ni to M ratio		Surface area ^c (m ² /gm)	Metal-oxide Reduction ^b (%)	H ₂ desorbed (μmole/g) ^{b,d}
	Ni	Cu or Fe	(Ni/M) ^a _{bulk}	(Ni/M) ^b _{XPS}			
Al ₂ O ₃	–	–	–	–	207	–	–
15Ni/Al ₂ O ₃	15.00	–	–	–	164	75	82
15Cu/Al ₂ O ₃	–	15.00	–	–	165	92	31
15Fe/Al ₂ O ₃	–	15.00	–	–	162	21	376
75Ni25Cu/Al ₂ O ₃	11.25	3.75	3.20	2.24	160	79	59
50Ni50Cu/Al ₂ O ₃	7.50	7.50	1.02	0.45	170	84	48
25Ni75Cu/Al ₂ O ₃	3.75	11.25	0.37	0.29	161	87	39
75Ni25Fe/Al ₂ O ₃	11.25	3.75	3.10	2.72	162	73	101
50Ni50Fe/Al ₂ O ₃	7.50	7.50	1.05	1.04	167	55	170
25Ni75Fe/Al ₂ O ₃	3.75	11.25	0.30	0.27	169	40	508

^a from XRF.

^b reduced catalysts.

^c calcined catalysts.

^d desorbed amount from Al₂O₃ has been subtracted.

was then cooled down to 323 K. After the temperature of the sample stabilized at 323 K the temperature was increased up to 1173 K at 10 K/min under a flow of 10% H₂/Ar (30 ml/min at STP). The variation in hydrogen consumption during reduction was monitored by the TCD and a H₂-TPR profile was obtained. The amount of H₂ consumed was determined from the H₂-TPR profile using calibration amounts of H₂ in Ar, which were then used to calculate the metal oxide reduction (%).

2.2.4. X-ray photoelectron spectroscopy (XPS)

X-ray photoelectron spectroscopy (XPS) was performed using a PHI 5000 Versaprobe II, FET Inc., Scanning XPS using Al Ka radiation ($\hbar\nu = 1486.6$ eV, spot size 200 μm, 45° collection angle, pass energy of analyzer 187.85 eV). The atomic concentration ratios were calculated by using CasaXPS program (Casa Software Ltd., UK) where surface area ratios were normalized with sensitivity factors based on Scofield cross sections. The following peaks were used for quantitative analysis of the corresponding metals: Ni 2p_{3/2}, Fe 2p_{3/2}, and Cu 2p_{3/2}.

2.2.5. Hydrogen-temperature programmed desorption (H₂-TPD)

The chemisorbed H₂ on the alumina support and reduced catalysts was analyzed by H₂-TPD using the above mentioned AMI-200 setup. Prior to H₂-TPD each sample was reduced *ex situ* in a down flow tubular quartz reactor at 823 K for 4 h in a flow of H₂. About 0.22 g of the reduced sample was taken in a U-shaped quartz reactor for the H₂-TPD study. The sample was again reduced at 823 K for 2 h and subsequently cooled to 313 K in a flow of H₂. Subsequently, the sample was held at 313 K for 0.5 h under the flow of Ar to remove weakly bound physisorbed hydrogen [36]. The desorption was carried out by increasing the temperature of the sample from 313 K to 773 K at 10 K/min and holding the temperature at 773 K for 0.5 h under the flow of Ar. As above the effluent gas was monitored by the TCD during temperature ramping and a H₂-TPD profile was obtained. The moles of desorbed H₂ were calculated by integrating the areas of the H₂-TPD profiles and using calibration pulses of premixed H₂ in Ar of known quantities. The moles of desorbed H₂ were used to determine the moles of surface metal sites, which were used to calculate the turnover frequency. The effect of hydrogen spillover on to the support was neglected by subtracting the H₂-TPD profile of the support from H₂-TPD profile of the catalysts. Furthermore, the effects of hydrogen spillover can be considered to be similar since the total metal loading was the same.

2.2.6. Transmission electron microscopy (TEM)

The transmission electron microscopy (TEM) images of the three catalysts (15Ni/Al₂O₃, 75Ni25Cu/Al₂O₃ and 75Ni25Fe/Al₂O₃) were obtained using a Tecnai G2 12 Twin (FEI) instrument equipped with a thermionic LaB6 electron source and operated at a primary electron energy of 120 kV. Prior to reduction, the three catalyst samples were crushed in a mortar into a fine powder. The reduced samples were then dispersed in an ethanol medium. The droplets of the ethanol suspension were placed onto a carbon coated Cu grid. The grid was then allowed to dry before loading the sample into the TEM instrument. Particle size was measured from the TEM images following previously reported procedures [37]. From the selected area electron diffraction (SAED) patterns lattice spacing was calculated. Both the particle size and lattice spacing were obtained by using the Gatan Microscopy Suite (GMS) 2 software, which was available with the instrument.

2.3. Reaction studies

The hydrogenation of CO₂ over the Al₂O₃ supported monometallic and bimetallic catalysts was performed in a tubular down-flow quartz reactor operating at 523 K and 1 atm. A thermocouple was placed inside the reactor and just above the catalyst bed to measure the reaction temperature. Prior to the reaction 100 mg of the calcined catalyst was reduced in a flow of H₂ (25 ml/min at STP) at 823 K for 4 h. After reduction, the reactor was cooled down to the desired reaction temperature under the same H₂ flow. The reactant gases containing 4% (v/v) CO₂ in H₂ with a total flow rate of 100 ml/min (STP) were premixed and passed through the reactor. Individual mass flow controllers were used to maintain the flow rates of the reactant gases. The molar composition of the unconverted feed and product gas stream was analyzed using a gas chromatograph (GC) (Nucon 5765) equipped with a Carbosphere column, a methanizer and a flame ionization detector (FID). Additional details of the reactor setup can be found in our previous work [36].

The catalyst amount and inlet molar flow rate were varied such that the conversions were maintained below 5% to ensure differential reactor conditions. Furthermore, the ratio of carbon atoms at the inlet of the reactor to carbon atoms at the outlet was better than ± 3%. Using the composition of the reactor outlet the conversion of CO₂, X_{CO₂}, and yield of CH₄ or CO, Y_{CH₄} or Y_{CO} were calculated using the formulae given below.

$$X_{CO_2} = \left(1 - \frac{F_{CO_2,out}}{F_{CO_2,out} + F_{CH_4,out} + F_{CO,out}}\right) \cdot 100\% \quad (1)$$

$$Y_{CH_4 \text{ or } CO} = \left(\frac{F_{CH_4, \text{out}} \text{ or } F_{CO, \text{out}}}{F_{CO_2, \text{out}} + F_{CH_4, \text{out}} + F_{CO, \text{out}}} \right) \cdot 100\% \quad (2)$$

Where, F_i was the molar feed rate of component i entering the reactor and expressed in mol/sec.

The reaction data were used to calculate the rate of CO_2 conversion, r_{CO_2} , in mol/g-cat/sec or mmol/mol-metal/sec using the formulae:

$$r_{CO_2} = \left(\frac{X_{CO_2}}{100} \right) \cdot \left(\frac{F_{CO_2}}{W_{\text{cat}}} \right) \text{ mol/g-cat/sec} \quad (3)$$

$$r_{CO_2} = \left(\frac{X_{CO_2}}{100} \right) \cdot \left(\frac{F_{CO_2}}{n_{\text{cat}}} \right) \text{ mmol/mol-metal/sec} \quad (4)$$

where, X_{CO_2} was the percentage CO_2 converted, F_{CO_2} was the molar feed rate of CO_2 entering the reactor and expressed in mol/sec, W_{cat} was the amount of catalyst and expressed in g, n_{cat} was total amount of metal present in the catalyst and expressed in mol. Such rate formulae are applicable for differential reactor conditions and were applied previously [19,23].

The turnover frequency (TOF) of CO_2 for this reaction TOF_{CO_2} was calculated for the different catalysts. The TOF_{CO_2} was defined as the number of CO_2 molecules converted over each surface metal site per second. The number of surface metal sites was determined from the H_2 -TPD data and assuming that one hydrogen atom was associated with a single metal site. The TOF_{CO_2} for each catalyst was calculated using the following formula [36].

$$TOF_{CO_2} = \left(\frac{F_{CO_2}}{W_{\text{cat}}} \right) \cdot \left(\frac{X_{CO_2}}{100} \right) \cdot \left(\frac{1}{M_s} \right) \text{ 1/sec} \quad (5)$$

where, M_s was the surface metal sites of the catalyst and expressed in mol/g-cat. In the similar way, turnover frequency of CH_4 , formed, TOF_{CH_4} , can be calculated by substituting X_{CO_2} with Y_{CH_4} .

2.4. Density functional theory calculations

Geometry optimization of the pristine surface was performed within the density functional theory framework using the Cambridge Sequential Total Energy Package (CASTEP) [38]. The generalized gradient approximation was used to include the exchange-correlation effects [39]. The exchange-correlation energy was described by the Perdew-Burke-Ernzerhof functional [40] and a plane wave cut-off energy of 360 eV was employed. The Brioullin-Zone sampling was done using $8 \times 8 \times 1$ k-points within Monkhorst-Pack scheme [41]. Effect of spin polarisation was considered to calculate the energies of the model surfaces, and the conjugate gradient algorithm was used to optimize the surfaces. The convergence threshold was set to 1.0×10^{-6} eV/atom for SCF, 1.0×10^{-6} eV/atom for energy, 0.01 eV/Å for maximum force, and 1.0×10^{-3} Å for maximum displacement.

The surface-slab model and low index closed packed surfaces were chosen to model the monometallic and bimetallic catalysts. The catalysts $15Ni/Al_2O_3$ and $75Ni25M/Al_2O_3$ ($M = Fe$ or Cu) were represented by $Ni(111)$ and $Ni_3M(111)$ surfaces. The monometallic and bimetallic surfaces were cleaved from an optimized Ni and Ni_3M fcc unit cell. The three surfaces were modelled by a four-layer slab with the bottom two layer fixed at their equilibrium bulk phase positions and the top two layers were allowed to relax. The surface-slab was represented by a $p(2 \times 2)$ supercell and a vacuum region of 12 Å was included. The reliability of the three bulk structure was evaluated by performing a XRD simulation using the Reflex module in Material Studio 6.0. (Software package of Accelrys Inc.), where an X-ray Diffractometer of $CuK\alpha_1$ ($\lambda_1 = 1.5405$ Å) was used to obtain the Bragg reflection from the three model structure.

3. Results and discussions

3.1. XRF and surface area analysis

The actual bulk Ni:M ratio was determined by XRF and reported in Table 1. The XRF data revealed that the actual and nominal bulk Ni:M ratios were similar. The nominal wt.% of metal (Ni and $M = Cu$, Fe) in the synthesized catalysts were determined and reported in Table 1 along with the surface areas of the calcined samples. Examination of Table 1 revealed that the surface area of the supported catalysts were lower than the support. This is due to the partial blocking of pores of the support by the metals impregnated over the support [42]. Furthermore, there was no specific trend in the measured surface area for the two series of supported catalysts. Similar results were reported previously [11,36].

3.2. X-ray diffraction patterns of calcined catalysts

X-ray diffraction patterns of calcined Al_2O_3 and Al_2O_3 supported samples were obtained and are shown in Fig. 1A and B. The diffraction pattern of Al_2O_3 is clearly visible in all the supported catalysts. The XRD patterns of $15Ni/Al_2O_3$, $Ni-Cu/Al_2O_3$ and $15Cu/Al_2O_3$ catalysts are shown in Fig. 1A, which revealed the presence of NiO and CuO phases in the calcined $15Ni/Al_2O_3$ and $15Cu/Al_2O_3$ samples, respectively. The cubic rock salt structure of NiO phase [43,44] and tenorite CuO phases [44,45] were identified. The $50Ni50Cu/Al_2O_3$ and $25Ni75Cu/Al_2O_3$ samples predominantly contained the features of the CuO phase, and the features of the NiO phase were dominant in $75Ni25Cu/Al_2O_3$. Interestingly, in the $50Ni50Cu$ sample the peaks of the NiO phase were shifted toward higher angles. These peak shifts were due to the formation of $NiCuO_x$; a solid solution formed between NiO and CuO species. A previous study on Al_2O_3 supported Ni-Cu bimetallic catalyst with a Ni to Cu ratio of 1:1 also suggested the formation of such solid solutions [46]. Formation of solid solutions in the $75Ni25Cu$ sample is not ruled out since the appearance of that solid solution phase may be restricted by the XRD detection limit. A previous study dealing with the thermodynamics of $NiO-CuO$ solid solutions reported that up to 30 mol% of CuO is soluble in NiO and a cubic rock salt phase is formed. For the range of 50–60 mol% of CuO the solid solution phase possess a tetragonal structure [44]. Thus, it is possible that $75Ni25Cu$ also possesses a cubic rock salt phase.

Fig. 1B revealed that two phases of iron oxide, Fe_2O_3 and Fe_3O_4 , were present in the $15Fe/Al_2O_3$ sample. The presence of the hematite phase of Fe_2O_3 and magnetite phase of Fe_3O_4 were consistent with previous studies [47,48]. Moreover, in the present study Fe_2O_3 was the more dominant phase present. In contrast, Fe_3O_4 phase was predominantly present in the Ni-Fe samples. The intensity of the Fe_3O_4 phase decreased as the Fe content decreased in the Ni-Fe samples. Thus, NiO , CuO , $NiCuO_x$, Fe_2O_3 and Fe_3O_4 phases were detected in the calcined supported Ni, Ni-M and M samples and the specific ratio of Ni to M controlled the amount of the corresponding oxide phases present.

3.3. Temperature programmed reduction analysis of calcined catalysts

The H_2 -TPR profiles of calcined Al_2O_3 supported Ni , Cu , Fe , $Ni-Cu$ and $Ni-Fe$ catalysts were obtained and are shown in Fig. 2A and B. The reduction profiles of Ni , $Ni-Cu$ and Cu samples are compared in Fig. 2A and those of Ni , $Ni-Fe$ and Fe in Fig. 2B. Three reduction features were observed for $15Ni/Al_2O_3$. The main reduction peak at ~ 820 K was attributed to the reduction of NiO to metallic Ni as suggested previously [36,49]. Two shoulders were also present at around 735 K and 1040 K of which the former had a larger intensity. Previous studies suggest that the two shoulders are due to different

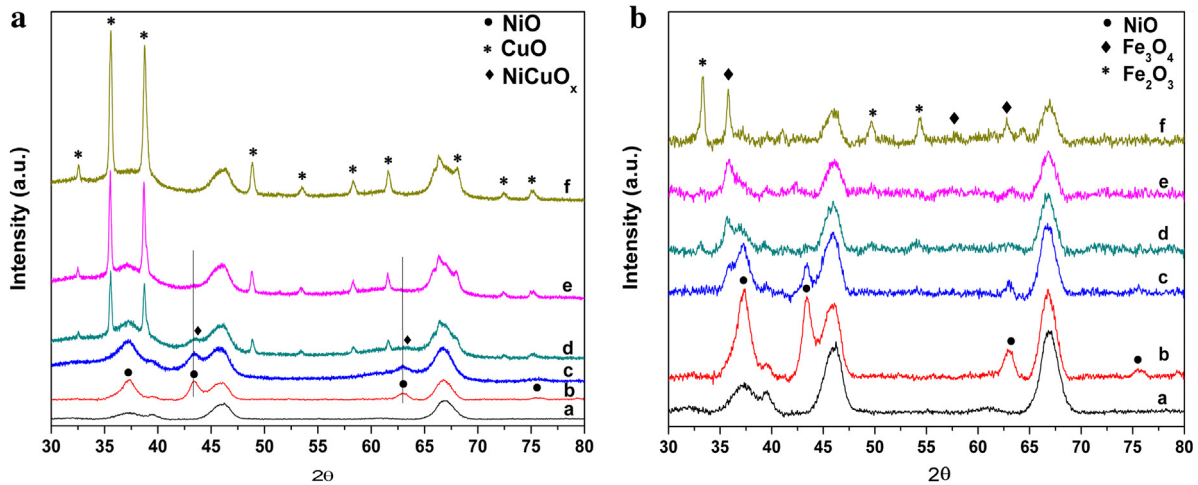


Fig. 1. (A) XRD patterns of calcined Al_2O_3 and Al_2O_3 supported Ni, Ni-Cu and Cu samples: (a) Al_2O_3 ; (b) 15Ni/ Al_2O_3 ; (c) 75Ni25Cu/ Al_2O_3 ; (d) 50Ni50Cu/ Al_2O_3 ; (e) 25Ni75Cu/ Al_2O_3 ; (f) 15Cu/ Al_2O_3 . (B) XRD patterns of calcined Al_2O_3 and Al_2O_3 supported Ni, Ni-Fe and Fe samples: (a) Al_2O_3 ; (b) 15Ni/ Al_2O_3 ; (c) 75Ni25Fe/ Al_2O_3 ; (d) 50Ni50Fe/ Al_2O_3 ; (e) 25Ni75Fe/ Al_2O_3 ; (f) 15Fe/ Al_2O_3 .

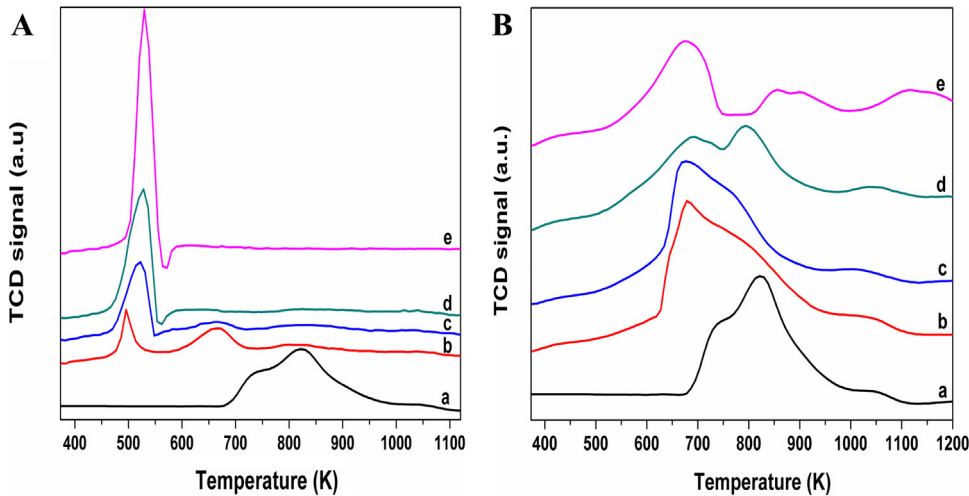


Fig. 2. (A) H_2 -TPR profile of calcined Al_2O_3 supported Ni, Ni-Cu and Cu samples: (a) 15Ni/ Al_2O_3 ; (b) 75Ni25Cu/ Al_2O_3 ; (c) 50Ni50Cu/ Al_2O_3 ; (d) 25Ni75Cu/ Al_2O_3 ; (e) 15Cu/ Al_2O_3 . (B) H_2 -TPR profile of calcined Al_2O_3 supported Ni, Ni-Fe and Fe samples: (a) 15Ni/ Al_2O_3 ; (b) 75Ni25Fe/ Al_2O_3 ; (c) 50Ni50Fe/ Al_2O_3 ; (d) 25Ni75Fe/ Al_2O_3 ; (e) 15Fe/ Al_2O_3 .

levels of NiO interaction with the Al_2O_3 support [11,46]. The former shoulder represents the reduction of trace amounts of NiO clusters or bulk NiO weakly interacting with the support [50]. The later shoulder might represent a stronger metal-support interaction that is due to a NiO species that is more difficult to reduce [50]. The 15Cu/ Al_2O_3 catalyst showed one sharp and well defined reduction peak at around 530 K, and this peak was attributed to the reduction of bulk CuO to metallic Cu as proposed previously [51]. The presence of such single, sharp peak might indicate greater homogeneity among the types of reducible copper oxide species. The absence of any high temperature reduction peak indicates that Cu_2O species was not present in the sample. This also suggests that there exists weaker interaction between the supported copper oxide species and the support matrix. The absence of the Cu_2O phase is consistent with the XRD pattern of the calcined 15Cu/ Al_2O_3 sample. The TPR profile of 75Ni25Cu/ Al_2O_3 and 50Ni50Cu/ Al_2O_3 were similar and contained three distinct peaks of different intensities. The initial sharp peak centered at approximately 495 K for the 75Ni25Cu sample appears to be due to the reduction of Cu(II) to Cu(0) of the CuO-NiO solid solution [46,52]. This initial peak shifted to relatively higher temperatures for the calcined 50Ni50Cu/ Al_2O_3 sample. The broad intermediate peak centered at around 662 K and observed

for both 75Ni25Cu and 50Ni50Cu samples was associated with the reduction of Ni(II) to Ni(0) as suggested by previous studies [46,52]. The final peak was also evident for both the Ni-Cu samples, and might be associated with the reduction of trace amounts of NiO species strongly interacting with the Al_2O_3 support [46]. The reduction profile of 25Ni75Cu/ Al_2O_3 was very similar to 15Cu/ Al_2O_3 , though the initial reduction peak was of lower intensity consistent with the lower amount of CuO present. Thus, sharper and well-defined reduction peaks characteristics of CuO reduction to Cu suggested homogeneity of the initial oxide present and weaker interaction of CuO with the support in the Cu rich Ni-Cu/ Al_2O_3 catalysts. The low temperature reduction peak observed in Ni rich Ni-Cu/ Al_2O_3 catalysts suggested the beneficial role of adding Cu in the Ni/ Al_2O_3 catalysts.

The H_2 -TPR profile of Ni, Ni-Fe and Fe samples were obtained and presented in Fig. 2B. The H_2 -TPR profiles were similar to those presented previously for a total metal loading of 10 wt.% [11]. The TPR profile of 15Ni/ Al_2O_3 is already discussed above. The 15Fe/ Al_2O_3 catalyst showed three main reduction peaks, each of which was relatively broad. The first peak centered at around 676 K is ascribed to the reduction of $\alpha\text{-Fe}_2\text{O}_3$ to $\alpha\text{-Fe}_3\text{O}_4$ [53,54]. The second peak (centered at about 880 K), having a smaller intensity

than the first one, appeared to be composed of two overlapping peaks of which the first peak referred to the reduction of Fe_3O_4 to FeO and the second one reflected the reduction of FeO to Fe [54]. Another work considered the occurrence of the overlapping peak due to the simultaneous reduction of iron oxides into metallic iron [53]. The third peak (~1120 K) was due to the interaction of FeO with Al_2O_3 as reported in the previous study [54]. The reduction features of 75Ni25Fe/ Al_2O_3 and 50Ni50Fe/ Al_2O_3 were similar and revealed a peak at about 675 K. A small shoulder was observed at high temperatures (>700 °C) for both the samples indicating stronger interaction with the support. The reduction peaks of these two Ni-Fe samples were shifted to lower temperatures relative to both the 15Ni/ Al_2O_3 and 15Fe/ Al_2O_3 samples. The reduction features of 25Ni75Fe/ Al_2O_3 revealed broad peaks due to the reduction of iron and nickel oxide phases. The overall shape of the TPR profile of the Ni-Fe and Fe catalysts was broad in nature, which suggests the heterogeneity in the oxidation states and the sites at which the iron species are located. Such type of observations were reported earlier for supported cobalt catalysts [55]. Furthermore, the reduction peaks of the Ni-Fe and Fe catalysts were at higher temperature than Ni-Cu and Cu catalysts indicating the higher reduction temperatures of Fe relative to Cu.

The metal oxide reduction (%) was calculated from the TPR profile using calculation procedures similar to those reported previously [54]. The corresponding data are tabulated in Table 1. For the monometallic component samples, the metal oxide reduction (%) of 15Cu/ Al_2O_3 was the highest at 92%, followed by 15Ni/ Al_2O_3 at 75%, and was the least for 15Fe/ Al_2O_3 at 23%. The metal oxide reduction (%) monotonically increased from 79% to 87% with increase in Cu content in the Ni-Cu samples. It appears that CuO, which was more easily reducible, promoted the NiO reduction in the bimetallic Ni-Cu samples. On the other hand, the metal oxide reduction (%) of Ni-Fe samples decreased from 73% to 40% when the Fe content increased in the catalysts. The decrease in metal oxide reduction (%) for the Ni-Fe samples appears to be related to the low metal oxide reduction (%) of supported Fe. Therefore, iron oxide being a less reducible species assists only in lowering the reduction temperature of the two calcined Ni-Fe/ Al_2O_3 samples; whereas, copper oxide (CuO) being more easily reducible species assists both in lowering the reduction temperature and increasing the overall metal oxide reduction (%).

The H_2 -TPR analysis for Al_2O_3 supported Ni, Cu, Fe, Ni-Cu and Ni-Fe have been studied previously [11,46,51–53,56]. However, unlike our studies such detailed comparative analysis with varying Ni:M ratio was not undertaken. The present study revealed that substituting a small amount of Ni (25%) with Fe or Cu in Ni-Fe or Ni-Cu bimetallic catalysts was beneficial in lowering the reduction temperature and keeping the metal oxide reduction (%) at comparable level.

3.4. X-ray diffraction patterns of reduced catalysts

The XRD patterns of Al_2O_3 and the two series of reduced Al_2O_3 supported Ni-M catalysts were obtained in the range of 30°–80°. However, to highlight the structural changes of the most intense metallic Ni peak in 15Ni/ Al_2O_3 , the XRD patterns are shown in the range of 40°–55° in Fig. 3A and B. The XRD patterns for the full range are included in the supplementary section as Fig. S1a and S1b. The XRD patterns of the Ni-Cu/ Al_2O_3 series catalysts are compared in Fig. 3A. The XRD patterns of 15Ni/ Al_2O_3 and 15Cu/ Al_2O_3 catalysts revealed the presence of metallic Ni peaks at 44.52° and 51.80° for 15Ni/ Al_2O_3 and Cu peaks at 43.3° and 50.4° for 15Cu/ Al_2O_3 . The metallic Ni and Cu phases are associated with the face-centered cubic structure [25,36,46,52]. Moreover, Fig. S1a showed the presence of metallic Ni and metallic Cu features at 76.40° and 74.06°, respectively. The three metallic Ni and metallic Cu features located

between 30° and 80° corresponded to the (111), (200) and (220) lattice planes. The absence of any NiO and CuO phases indicates that significant reduction of the corresponding metal oxides has occurred. The two Ni-Cu catalysts, namely 75Ni25Cu/ Al_2O_3 and 50Ni50Cu/ Al_2O_3 , showed broad peaks at 44.17° and 43.90°. These two peaks shifted progressively towards smaller 2θ angles relative to the metallic Ni peak position at 44.52° as the Cu content increased in the two Ni-Cu catalysts. This shift indicates the formation of Ni-Cu alloy (or Ni rich Ni-Cu alloy) [26,56]. The composition of the alloy in the above two Ni-Cu catalysts could be of the form $\text{Ni}_{1-x}\text{Cu}_x$ (Ni-Cu solid solution), where x depends on the initial loading. Previous studies with different supports and loadings also indicated the formation of such $\text{Ni}_{1-x}\text{Cu}_x$ alloy in supported bimetallic Ni-Cu catalysts [46,52]. The 2θ position of the $\text{Ni}_{1-x}\text{Cu}_x$ alloy phase is between that of metallic Ni and Cu phases, and consistent with the Ni-Cu alloy available in the PCD library [57,58]. Interestingly, 50Ni50Cu/ Al_2O_3 also contained a sharp diffraction peak at a 2θ position similar to that of metallic Cu phase. This sharp peak indicates that Cu phase is present along with the $\text{Ni}_{1-x}\text{Cu}_x$ alloy in the 50Ni50Cu/ Al_2O_3 catalyst, which suggests segregation of Cu atoms. It is worthwhile noting that the absence of metallic Cu phase in the 75Ni25Cu/ Al_2O_3 catalyst does not guarantee the nonexistence of small domains of segregated Cu atoms in this sample. Meanwhile, the chemical formula associated with such alloy phases was estimated to be of $\text{Ni}_{0.75}\text{Cu}_{0.25}$ and $\text{Ni}_{0.5}\text{Cu}_{0.5}$.

The XRD patterns of the reduced Ni-Fe series catalysts are compared in the 40°–55° region in Fig. 3B. The metallic Fe peak was observed in the XRD pattern of 15Fe/ Al_2O_3 catalyst at 44.73°. Unlike the 15Ni/ Al_2O_3 and 15Cu/ Al_2O_3 catalysts, peaks for the iron oxide phase (Fe_3O_4) were also observed (shown in Fig. S1b) suggesting incomplete reduction. The presence of Fe_3O_4 in the reduced catalyst was consistent with the low metal oxide reduction (%) obtained from H_2 -TPR study of this sample discussed above. The bimetallic 75Ni25Fe/ Al_2O_3 catalyst possessed a peak at 44.27°, which was slightly shifted from the metallic Ni peak at 44.52°. Similar shifts towards smaller 2θ angles were also reported previously due to the possible formation of Ni_3Fe alloy [11]. The other two bimetallic Ni-Fe samples contained diffraction peaks at gradually decreasing 2θ positions as the Ni content in the catalyst decreased. These peaks were also attributed to Ni-Fe alloys other than Ni_3Fe [11,37,53]. Interestingly, the absence of any metallic Fe peak in the 50Ni50Fe/ Al_2O_3 catalyst indicates that no “free” Fe was detected in this catalyst. Unlike the peak position of the $\text{Ni}_{1-x}\text{Cu}_x$ alloy phase, the position of the Ni-Fe alloy phases was not situated between the 2θ positions of the metallic Ni and metallic Fe phase. Thus, XRD patterns reveal that different types of Ni-M alloys appear to be formed in the two series of Ni-M/ Al_2O_3 catalysts.

3.5. X-ray photoelectron spectroscopy of reduced catalysts

The average surface Ni to M (M = Cu or Fe) ratios as measured from XPS is reported in Table 1 along with calculated bulk Ni to M ratios. The data in Table 1 reveals that there was a difference between the XPS determined surface Ni/Cu ratio and bulk Ni/Cu ratio for Ni/Cu nominal ratio ≥ 1 in the Ni-Cu/ Al_2O_3 catalysts. The lower $(\text{Ni}/\text{Cu})_{\text{XPS}}$ ratio suggests that Cu atoms segregate to the surface. Similar surface enrichment with Cu for Ni-Cu/ SiO_2 catalysts was also shown previously [59]. However, previous study also showed significant copper enrichment at region with lower Ni content than copper. In contrast, our results show that copper enrichment is not significant at lower Ni content. It appears that the large majority of copper particles in the Cu rich Ni-Cu catalyst (25Ni75Cu/ Al_2O_3) might hamper additional Cu atoms to diffuse to the surface. Moreover, the XRD pattern of this catalyst did not show any alloy peak. In contrast, all the Ni-Fe/ Al_2O_3 catalysts possessed almost similar surface and bulk Ni/Fe ratios. A

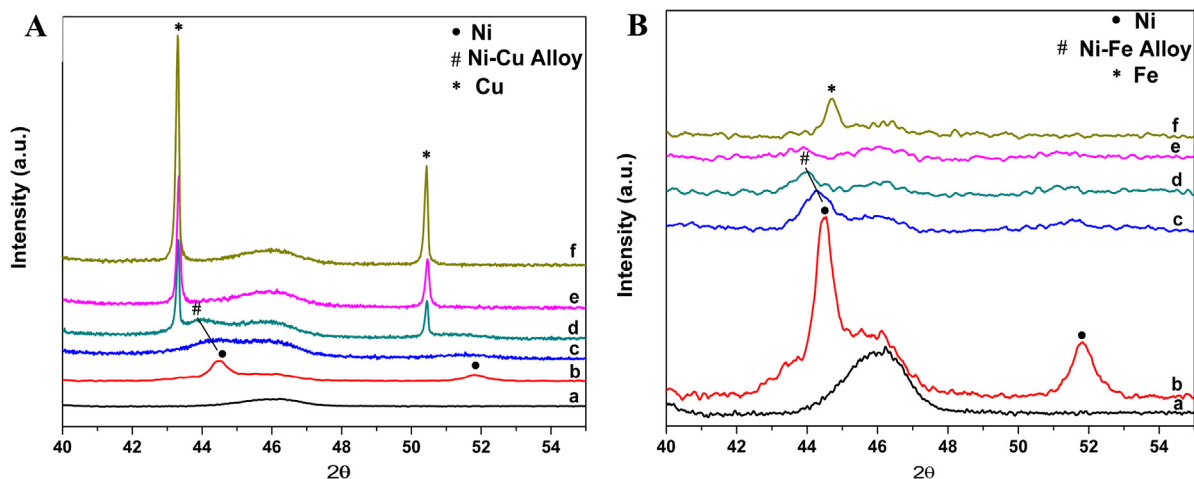


Fig. 3. (A) XRD patterns of reduced Al₂O₃ and Al₂O₃ supported Ni, Ni-Cu and Cu samples: (a) 15Ni/Al₂O₃; (b) 75Ni25Cu/Al₂O₃; (c) 50Ni50Cu/Al₂O₃; (d) 25Ni75Cu/Al₂O₃; (e) 15Cu/Al₂O₃; (f) Al₂O₃. (B) XRD patterns of reduced Al₂O₃ and Al₂O₃ supported Ni, Ni-Fe and Fe samples: (a) 15Ni/Al₂O₃; (b) 75Ni25Fe/Al₂O₃; (c) 50Ni50Fe/Al₂O₃; (d) 25Ni75Fe/Al₂O₃; (e) 15Fe/Al₂O₃; (f) Al₂O₃.

"slight" surface enrichment for Ni-Fe systems has been observed by XPS for a Ni76%/Fe24% (100) surface by Brundle et al. [60]. The small difference between the Ni and Fe surface energies (2.45 J/m² at 0 K and 2.55 J/m² at 0 K respectively) [61] and the lower surface energy of Cu than Ni (1.85 J/m² at 0 K and 2.45 J/m² at 0 K, respectively) [61] appears to be the reason for the surface enrichment of Cu in the Ni-Cu/Al₂O₃ catalysts and the absence of enrichment in the Ni-Fe/Al₂O₃ catalysts.

3.6. Hydrogen-temperature programmed desorption of reduced catalysts

The H₂-TPD profile of the reduced Al₂O₃ support and Al₂O₃ supported catalysts were obtained in the temperature range from 323 to 773 K. The H₂-TPD profile of the Al₂O₃ support was subtracted from that of the supported catalysts to enable better comparison and the resulting profiles are shown in Fig. 4A and B. The H₂-TPD profiles of 15Ni/Al₂O₃ and 15Cu/Al₂O₃ shown in Fig. 4A contained only one desorption peak at 378 and 390 K, respectively. A desorption peak present at a higher temperature suggests more strongly bound hydrogen species on the Cu surface. Besides the difference in the position of the desorption peak the profiles of these two catalysts were similar. Similar increase in the position of the desorption peak maxima was also reported for TiO₂ supported Cu and Ni catalysts [62]. The TPD profiles of 75Ni25Cu/Al₂O₃ and 50Ni50Cu/Al₂O₃ also had a single desorption peak, and the position of the desorption peak shifted toward higher temperatures with increasing Cu content compared to 15Ni/Al₂O₃. These results are in contrast to those of the previous work, which reported a lowering of the position of the H₂-TPD maxima for Ni-Cu bimetallic catalysts relative to their monometallic counterparts [62]. The difference between the present work and those reported previously may be due to the Al₂O₃ supported catalyst used in the present study and the TiO₂ supported catalysts used in the previous study. The TPD profile of 25Ni75Cu/Al₂O₃ resembled the profile of the 15Cu/Al₂O₃ catalyst.

The H₂-TPD profiles of 15Ni/Al₂O₃, Ni-Fe/Al₂O₃ and 15Fe/Al₂O₃ are compared in Fig. 4B. The desorption of H₂ for the 15Fe/Al₂O₃ catalyst occurred at a much higher temperature (509 K) relative to the 15Ni/Al₂O₃ catalyst. A small shoulder at 426 K was also observed for 15Fe/Al₂O₃. A previous study on SiO₂ supported Fe catalyst also reported a H₂-TPD desorption peak maxima at higher temperature [63]. This indicates that hydrogen is strongly bound to the Fe surface sites. The H₂-TPD profile of 75Ni25Fe/Al₂O₃ and 50Ni50Fe/Al₂O₃ contained a single desorption peak at 401 and 391 K, respectively.

These peaks were also shifted towards higher temperature relative to 15Ni/Al₂O₃. These shifts appear to be due to the influence of the Fe atoms on the alloy surface sites. As the atomic radii and the surface energy of Ni and Fe are similar it is expected that the alloy formed would be homogeneous and the peaks migrating to higher temperature is indicative of the presence of strong Fe binding sites. In contrast, the TPD profile of 25Ni75Fe/Al₂O₃ was similar to 15Fe/Al₂O₃; however, an additional small peak (350 K) was also detected. It appears that the majority of the surface sites are Fe atoms and the small peak with lower intensity at 350 K might be associated with Ni containing sites.

The amounts of chemisorbed H₂ on the supported catalysts under both series were calculated from the H₂-TPD data and are reported in Table 1. The amount of chemisorbed H₂ was observed to be the highest for 15Fe/Al₂O₃, followed by a large drop for 15Ni/Al₂O₃ and it was the least for 15Cu/Al₂O₃. A monotonic decrease in the amount of chemisorbed H₂ with increasing Cu in the samples was observed for the series of Ni-Cu/Al₂O₃ catalysts. A previous study also reported a monotonic decrease in the amount of chemisorbed CO on SiO₂ supported Ni-Cu catalysts with increasing Cu content in the catalysts [46]. The decrease in the amount of chemisorbed H₂ amount suggested that the number of surface sites gradually decreased. Specifically, the dispersion would continually decrease in Ni-Cu catalysts and become the lowest for the supported Cu catalyst. Similar results were obtained previously, irrespective of support used in the catalyst and probe molecule chosen for chemisorption [46,59,62]. In contrast, the amount of chemisorbed H₂ for the Ni-Fe/Al₂O₃ catalysts was much larger than on the Ni-Cu samples. Similar increase in amount of hydrogen adsorbed on Ni-Fe containing catalyst was reported previously [63]. The increase in chemisorbed H₂ for the Ni-Fe/Al₂O₃ catalysts with increasing Fe content suggested the availability of more surface sites [11]. Thus, the surface alloy sites present in the two Ni-M/Al₂O₃ series of catalysts are different.

3.7. Catalytic performance for CO₂ hydrogenation

The CO₂ hydrogenation reaction was carried out over the Al₂O₃ support and Al₂O₃ supported catalysts at 523 K and 1 atm pressure. No reaction occurred on the Al₂O₃ support under these conditions. Each supported catalyst was active for this reaction. The products formed were CH₄ and CO. Based on the amounts of CH₄ and CO formed, the reactivity data was calculated and reported in Table 2, which includes rates of CO₂ converted (g-mol/g-cat/sec

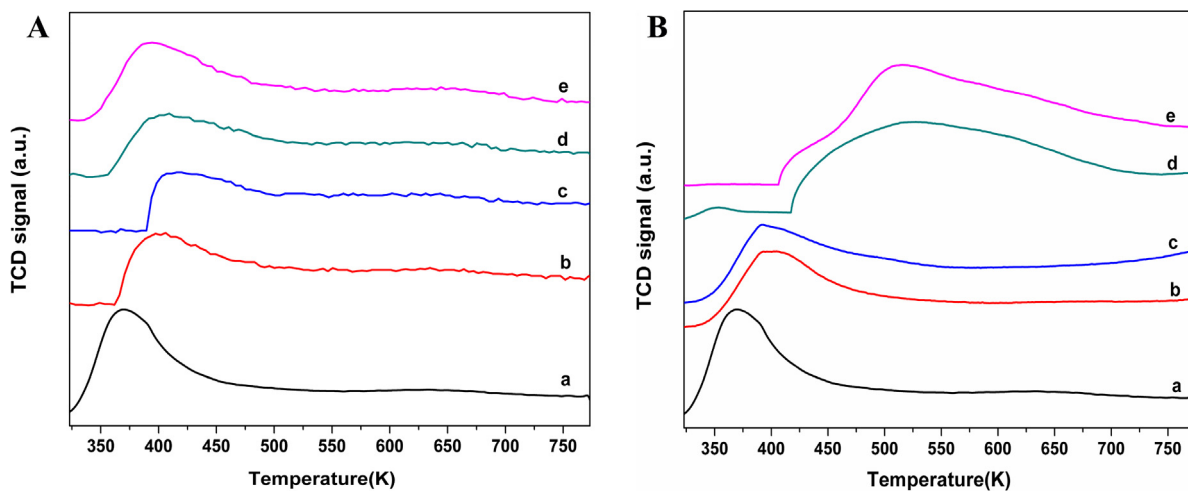


Fig. 4. (A) H_2 -TPD profile of reduced Al_2O_3 supported Ni, Ni-Cu and Cu samples: (a) $15\text{Ni}/\text{Al}_2\text{O}_3$; (b) $75\text{Ni}25\text{Cu}/\text{Al}_2\text{O}_3$; (c) $50\text{Ni}50\text{Cu}/\text{Al}_2\text{O}_3$; (d) $25\text{Ni}75\text{Cu}/\text{Al}_2\text{O}_3$; (e) $15\text{Cu}/\text{Al}_2\text{O}_3$. The H_2 -TPD profile of the Al_2O_3 support was subtracted from the profile of each sample. (B) H_2 -TPD profile of reduced Al_2O_3 supported Ni, Ni-Fe and Fe samples: (a) $15\text{Ni}/\text{Al}_2\text{O}_3$; (b) $75\text{Ni}25\text{Fe}/\text{Al}_2\text{O}_3$; (c) $50\text{Ni}50\text{Fe}/\text{Al}_2\text{O}_3$; (d) $25\text{Ni}75\text{Fe}/\text{Al}_2\text{O}_3$; (e) $15\text{Fe}/\text{Al}_2\text{O}_3$. The H_2 -TPD profile of the Al_2O_3 support was subtracted from the profile of each sample.

Table 2
Reactivity data (rate and TOF) for CO_2 hydrogenation using $15\text{Ni}/\text{Al}_2\text{O}_3$, $\text{Ni}-\text{M}/\text{Al}_2\text{O}_3$ and $\text{M}/\text{Al}_2\text{O}_3$ catalysts. $\text{M} = \text{Cu}$ or Fe . Reaction conditions: $\text{CO}_2:\text{H}_2 = 1:24$, $w_{\text{cat}} = 0.1\text{ g}$ and reaction temperature = 523 K.

Sample nomenclature	Reaction rate in		$\text{TOF}_{\text{CO}_2}(\text{s}^{-1}) \times 10^3$	$\text{TOF}_{\text{CH}_4}(\text{s}^{-1}) \times 10^3$
	$\text{g}\text{-mol/g-cat/sec} \times 10^6$	$\text{mmol/mol metal/sec}$		
$15\text{Ni}/\text{Al}_2\text{O}_3$	1.07 ± 0.08	0.42 ± 0.03	13.1 ± 1.01	13.1 ± 1.01
$15\text{Cu}/\text{Al}_2\text{O}_3$	0.10 ± 0.01	0.04 ± 0.01	2.87 ± 0.20	0.31 ± 0.06
$15\text{Fe}/\text{Al}_2\text{O}_3$	0.15 ± 0.01	0.06 ± 0.01	0.40 ± 0.02	0.11 ± 0.01
$75\text{Ni}25\text{Cu}/\text{Al}_2\text{O}_3$	0.38 ± 0.01	0.15 ± 0.01	6.39 ± 1.10	3.54 ± 0.80
$50\text{Ni}50\text{Cu}/\text{Al}_2\text{O}_3$	0.23 ± 0.02	0.09 ± 0.03	4.83 ± 1.00	1.51 ± 0.60
$25\text{Ni}75\text{Cu}/\text{Al}_2\text{O}_3$	0.21 ± 0.02	0.09 ± 0.03	5.27 ± 1.10	1.07 ± 0.50
$75\text{Ni}25\text{Fe}/\text{Al}_2\text{O}_3$	3.39 ± 0.23	1.31 ± 0.09	33.6 ± 2.31	32.8 ± 2.30
$50\text{Ni}50\text{Fe}/\text{Al}_2\text{O}_3$	0.72 ± 0.01	0.27 ± 0.01	4.21 ± 0.70	3.72 ± 0.80
$25\text{Ni}75\text{Fe}/\text{Al}_2\text{O}_3$	0.33 ± 0.03	0.12 ± 0.01	0.65 ± 0.06	0.43 ± 0.05

and $\text{mmol/mol metal/sec}$), TOF_{CO_2} and TOF_{CH_4} . The reactivity data reported in Table 2 are the average of several runs conducted and the standard errors associated with the rates and TOF are given. Among the supported monometallic catalysts, the rate of CO_2 converted was the highest for $15\text{Ni}/\text{Al}_2\text{O}_3$, 1.07×10^{-6} mol/g-cat/sec, and the least for $15\text{Cu}/\text{Al}_2\text{O}_3$, 1.00×10^{-7} mol/g-cat/sec. The $15\text{Fe}/\text{Al}_2\text{O}_3$ catalyst was also less active relative to $15\text{Ni}/\text{Al}_2\text{O}_3$ and the rate of CO_2 converted was 1.50×10^{-7} mol/g-cat/sec. The three $\text{Ni}-\text{Cu}/\text{Al}_2\text{O}_3$ catalysts had lower rates of CO_2 conversion compared to $15\text{Ni}/\text{Al}_2\text{O}_3$. The drop in rates of CO_2 conversion for the $\text{Ni}-\text{Cu}/\text{Al}_2\text{O}_3$ catalysts with decreasing Ni content till $15\text{Cu}/\text{Al}_2\text{O}_3$ was not proportional to the decrease in the Ni content. The XPS data in Table 1 reveals that the surface was enriched with Cu for most of the $\text{Ni}-\text{Cu}$ catalysts. Thus, due to the formation of relatively inactive alloys and surface enrichment of inactive Cu the catalytic activity dropped disproportionately.

A more detailed analysis of the rate data revealed that the catalytic activity of CO_2 hydrogenation is promoted when 25% of Ni is substitute with Fe. This promotional effect was not observed for the other Ni-Fe and all the Ni-Cu catalysts. The improved rate observed for $75\text{Ni}25\text{Fe}/\text{Al}_2\text{O}_3$ is attributed to the presence of the Ni_3Fe alloy in the catalyst as detected by XRD. Similar conclusions were reported previously [19,23]. The presence of Ni_3Fe alloy was also revealed from the Mossbauer spectra of similar catalyst [24]. The other Ni-Fe catalysts also contained Ni-Fe alloys that were different from Ni_3Fe , but the activity was less than pure Ni catalyst. The decrease in catalytic activity in other Ni-Fe catalysts ($50\text{Ni}50\text{Fe}/\text{Al}_2\text{O}_3$ and $25\text{Ni}75\text{Fe}/\text{Al}_2\text{O}_3$) may be due to: (i) the lower amount of Ni containing sites, (ii) formation of an Ni-Fe alloy that

possessed a lower activity, and/or the (ii) majority of surface sites were Fe, which is known to form more CO than CH_4 [64]. Thus, a specific amount of Fe substitution in $\text{Ni}/\text{Al}_2\text{O}_3$ catalyst is more beneficial than Cu substitution for CO_2 hydrogenation.

3.8. Transmission electron microscopy (TEM)

To investigate if any significant differences in the particle sizes exist and to ascertain the formation of alloys in the reduced $\text{Ni}-\text{M}/\text{Al}_2\text{O}_3$ catalysts, TEM images were acquired for $15\text{Ni}/\text{Al}_2\text{O}_3$, $75\text{Ni}25\text{Cu}/\text{Al}_2\text{O}_3$ and $75\text{Ni}25\text{Fe}/\text{Al}_2\text{O}_3$ catalysts. The Fig. 5(a-c) show representative TEM images of $15\text{Ni}/\text{Al}_2\text{O}_3$, $75\text{Ni}25\text{Cu}/\text{Al}_2\text{O}_3$ and $75\text{Ni}25\text{Fe}/\text{Al}_2\text{O}_3$ catalysts, respectively. A large irregular feature, which is observed on a lighter background in these images, is attributed to the Al_2O_3 supported material and the brighter background corresponds to the vacuum in the microscope. Smaller, approximately circular, darker areas are observed within Al_2O_3 , which are attributed to the Ni and Ni-M phases. The SAED pattern of each of the catalysts was obtained and shown in Fig. 5(a-c). The concentric ring pattern suggested that Ni and Ni-M phases were polycrystalline in nature. The distances measured on the ring patterns of $15\text{Ni}/\text{Al}_2\text{O}_3$ catalyst indicated the (111), (200) and (220) lattice planes. For example, a distance of 2.04 \AA measured on the first ring of Ni correspond to the (111) lattice plane. The lattice spacing with respect to first ring increased for the $75\text{Ni}25\text{Fe}$ and $75\text{Ni}25\text{Cu}$ catalysts. The distance measured was 2.06 for both the catalysts. Such increase in the lattice spacing is possibly due to formation of alloy between Ni and M ($\text{M} = \text{Cu}/\text{Fe}$). The values obtained in our study matched reasonably well with the reference lattice dis-

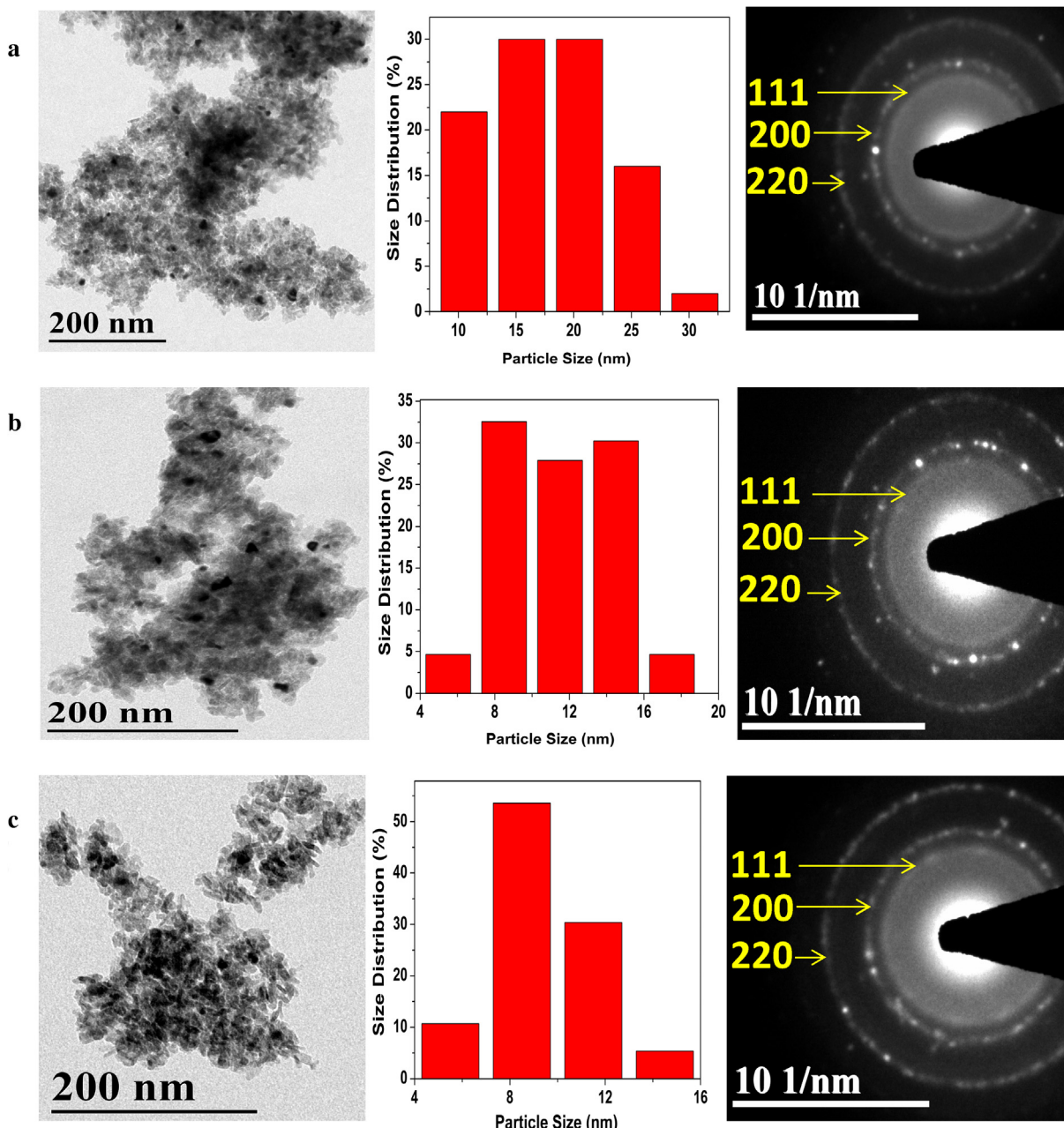


Fig. 5. TEM image, corresponding size distribution histogram and the corresponding SAED pattern of the Ni and Ni-M catalysts: (a) 15Ni/Al₂O₃, (b) 75Ni25Cu/Al₂O₃, (c) 75Ni25Fe/Al₂O₃.

tances for: Ni(111), 2.034 Å [37]; Ni-Fe (111) alloys, 2.0–2.1 Å [37]; Ni-Cu (200) alloys, ~1.78 Å [65]; Cu(111), 2.087 Å [26]; Fe(110), 2.0 Å [37]. Since the XRD patterns showed absence of metallic and unalloyed Cu or Fe in the 75Ni25Cu or 75Ni25Fe catalysts and a single peak due to the Ni-M (111) phase in the 75Ni25 M catalysts, it is most likely that Ni and M in the two 75Ni25 M catalysts formed an alloy. Moreover, the alloy retained the face centered cubic structure as the concentric rings in the SAED patterns of the two 75Ni25 M catalysts are due to the (111), (200) and (220) planes.

Particle size distributions based on TEM images of the Ni/Al₂O₃ and 75Ni25 M/Al₂O₃ samples are presented as histograms in Fig. 5(a–c). It was observed that the particle size distribution for Ni/Al₂O₃ catalyst is broad compared to the two alloy catalysts. The average particle size is 16 nm for 15Ni/Al₂O₃, 10 nm for 75Ni25Cu/Al₂O₃ and 9 nm for 75Ni25Fe/Al₂O₃ catalysts. These values are reported in Table 3 for comparison. Therefore, substi-

tution of M (Cu or Fe) in Ni/Al₂O₃ catalyst decreases the average particle size. The particle size distribution and the average particle sizes of several Ni-Fe bimetallic catalysts have been reported previously for different metal loading and a similar trend was observed [37]. The decrease in average particle size for the Ni-Cu/Al₂O₃ compared to Ni/Al₂O₃ observed in our study followed a similar trend as those reported previously, where TiO₂ was used as support [62]. A decrease in crystallite size for the two Ni-M alloy catalysts compared to Ni was also observed from the XRD patterns. The metal/alloy crystallite sizes were determined by applying the Scherrer equation for the most intense peak in the XRD pattern for the three catalysts, 15Ni/Al₂O₃, 75Ni25Cu/Al₂O₃ and 75Ni25Fe/Al₂O₃. Such method was previously applied to calculate the crystallite size of the reduced supported catalyst [11,36,37,53]. The crystallite size calculated for these catalysts are also reported in Table 3. The data showed that the crystallite size of Ni metal

Table 3Structural properties of 15Ni/Al₂O₃ and 75Ni25 M/Al₂O₃ catalysts. M = Cu or Fe.

Catalysts	Crystallite size (nm)	Particle size (nm)	Optimized lattice constant (Å)		2θ hkl (111)	
			simulation	experimental	simulation	experimental
15Ni/Al ₂ O ₃	13	16	3.536	3.525	44.32	44.52
75Ni25Cu/Al ₂ O ₃	7	10	3.556	3.548	44.05	44.17
75Ni25Fe/Al ₂ O ₃	8	9	3.551	3.541	44.14	44.25

was 13 nm, which was larger than the two 75Ni25 M alloy catalysts. The two 75Ni25 M/Al₂O₃ catalysts containing Ni-Cu and Ni-Fe alloy possessed crystallite sizes of 7 nm and 8 nm respectively. It appears that the volume average crystallite size observed by XRD were similar to the number average particle size observed by TEM over the three catalysts.

To account for the difference in average particle sizes while comparing the catalytic activity, the TOF_{CO₂} and TOF_{CH₄} were calculated. Both turnover frequencies were calculated using the number of surface metal sites estimated from the H₂-TPD studies and given in Table 1. The TOF_{CO₂} and TOF_{CH₄} calculated for all the catalysts are also reported in Table 2. The maximum TOF_{CO₂} of 33.6×10^{-3} s⁻¹ was observed when 75Ni25Fe/Al₂O₃ was used as the catalyst. In comparison the TOF_{CO₂} for 15Ni/Al₂O₃ was 13.1×10^{-3} s⁻¹ and for 15Fe/Al₂O₃ was 0.4×10^{-3} s⁻¹. The TOF_{CO₂} for the Ni-Fe and Fe catalysts ranged from 0.4×10^{-3} to 33.6×10^{-3} s⁻¹ and for Ni-Cu and Cu catalysts, the values ranged from 2.9×10^{-3} to 6.4×10^{-3} s⁻¹. The large differences in rates of CO₂ conversion and number of surface metal sites gave rise to a larger span in the TOF_{CO₂} values for the Ni-Fe series catalysts; whereas, the proximity in rates of CO₂ conversion and number of surface sites observed for the Ni-Cu series catalysts led to a relatively smaller span in TOF_{CO₂} values.

The TOF_{CO₂} of 15Ni/Al₂O₃ reported in the present study was very close to those observed previously for a commercial Ni catalysts of 23 wt.% at 523 K [20]. Furthermore, a recent study used a commercial 20% Ni/Al₂O₃ catalyst for the CO₂ hydrogenation reaction in the presence of excess hydrogen and provided the rate of CH₄ formation [16], which was similar to the rate of CO₂ conversion observed in the present study. The reported rate is essentially equal to the rate of CO₂ conversion for the Ni/Al₂O₃ catalyst in our study as CO was not detected. Similar enhancement in rates were also previously reported for a nominal total metal loading of 10 and 30 wt.% and a reduction temperature of 773 K [11]. In the present study the total metal loading was 15 wt.% and reduction temperature was 823 K. A higher reduction temperature of 823 K was required to ensure significant reduction of the calcined catalysts and in line with another study dealing with supported Ni and Ni-Fe catalysts [23]. An improvement in rate was also previously observed for the CO₂ hydrogenation reaction when a Ni-Fe catalysts supported on Al₂O₃ containing a total metal loading of 25 wt.% was used [23]. In that study the maximum rate (mmol/mol-metal/sec) was observed for the catalyst containing 75% Ni and 25% Fe and the rate of this catalyst was higher than the supported Ni catalyst by a factor of 1.5. In the present study the measured rate for 75Ni25Fe/Al₂O₃ is almost 3.2 times higher than 15Ni/Al₂O₃. Although the rates reported in the previous study were about one order of magnitude higher than the present study, the trend in rates was similar. The higher rates in the previous study could be due to the higher total metal loading and different experimental conditions used.

The TOF_{CH₄} was also calculated for all the catalysts and the data shows that for the Ni-Fe catalysts TOF_{CO₂} and TOF_{CH₄} were in close proximity. The closeness of the two turnover frequency values suggests that on Ni-Fe catalysts the formation of CH₄ is more favoured than CO. However, by comparing the TOF_{CO₂} and TOF_{CH₄} values for 15Fe/Al₂O₃ it is clear that the formation of CO is more favoured than CH₄. In contrast, the TOF_{CO₂} and TOF_{CH₄} values for the Ni-Cu catalysts were significantly different and the formation of CO was

Table 4

d-projected density of states (d-PDOS) based electronic properties of Ni in pure Ni and Ni alloy surfaces.

Catalysts	Surface	d-band center ε_d (eV)	d-DOS at E _F , N _{E_F}
15Ni/Al ₂ O ₃	Ni(111)	-1.28	5.73
75Ni25Cu/Al ₂ O ₃	Ni ₃ Cu(111)	-1.07	6.11
75Ni25Fe/Al ₂ O ₃	Ni ₃ Fe(111)	-1.30	2.91

more favoured than CH₄. The predominant formation of CO in the Ni-Cu catalysts was in-line with the XPS results, which suggested that Cu segregated to the surface. A previous study dealing with supported Fe and Cu catalysts for CO₂ hydrogenation also showed that the CO formation was more favoured than CH₄ [64,66].

Therefore, the present study revealed that improvement in rate of CO₂ conversion, TOF_{CO₂}, and TOF_{CH₄} during CO₂ hydrogenation occurred in the 75Ni25Fe/Al₂O₃ catalyst relative to pure Ni/Al₂O₃ and the improvement is due to alloy formation. Furthermore, in the 75Ni25Fe/Al₂O₃ catalyst the Ni to Fe ratio was 3:1, similar to that expected in the Ni₃Fe alloy. For the same Ni to Cu ratio in the Ni-Cu/Al₂O₃ catalyst, formation of suitable Ni-Cu alloy of the type Ni_{1-x}Cu_x was evident; however, the corresponding catalyst (75Ni25Cu/Al₂O₃) showed a decrease in rate of CO₂ conversion and turnover frequencies relative to Ni/Al₂O₃. Furthermore, the degree of reduction of these two Ni-M catalysts was similar. Thus, it is meaningful to characterize the surface of the two different types of alloy catalysts along with pure Ni using DFT calculations. Density Functional Theory calculations are particularly suitable for characterizing the electronic structure of alloy catalysts [27–31].

3.9. Density functional theory calculations on bulk and surface structure

The three catalysts 15Ni/Al₂O₃, 75Ni25Cu/Al₂O₃ and 75Ni25Fe/Al₂O₃ were modelled for their bulk and surface structure of the unsupported monometallic and bimetallic systems and the results are described in this section. Though the (Ni/Cu)_{XPS} ratio for 75Ni25Cu/Al₂O₃ showed some amount of surface segregation of Cu the majority of the surface was due to the Ni_{1-x}Cu_x alloy. The three bulk models used to represent the supported metal and alloy sites corresponded to the fcc structure, which was in accordance with the XRD results on these reduced catalysts. For the two alloy catalysts in their bulk fcc structure, the corner positions are occupied by the guest metal atom (Fe or Cu) and the face centered positions are occupied by Ni metal atoms. This atomic arrangement led to the formation of Ni₃M (M = Cu, Fe) alloy structure, which corresponds to the 75Ni25 M composition in the synthesized catalysts. Since the atomic weights of the three metals are similar the formation of Ni₃M should be acceptable. Although the 75Ni25Cu/Al₂O₃ catalyst possessed Ni_{1-x}Cu_x type of Ni-Cu alloy, to compare and derive properties the structure was assumed to be similar to Ni₃Fe.

The three bulk structures were optimized and their optimized lattice constants are reported in Table 3. The optimized lattice constant of the bulk alloy reported in the table increased relative to bulk Ni. Moreover, bulk Ni₃Cu possessed a relatively higher lattice constant than bulk Ni₃Fe. The calculated lattice constant of the

monometallic Ni bulk unit cell matched reasonably with previous studies [67,68]. The increase in lattice constant of the bulk alloy relative to bulk Ni is also consistent with the previous findings [69,70]. The three characteristic reflections [(111), (200), (220)] of the fcc Ni and Ni₃M alloys were obtained and the 2θ position of the characteristic (111) reflection was compared with the experimental XRD patterns in Table 3. It was observed that the simulated and experimental peak shifts are in close correspondence. Thus, relative peak shift for each reflection is a characteristic feature of alloy structure and are consistent with the formation of alloys observed in the supported catalysts.

The three bulk models were then cleaved to form the Ni(111), Ni₃Fe(111) and Ni₃Cu(111) surfaces. A rectangular (2 × 2) supercell with 4 metal atoms per layer was used to represent each surface. For Ni₃Cu(111) and Ni₃Fe(111), each layer contained three Ni and one M metal atom. The three surfaces were relaxed and subsequently the d projected density of states (d-PDOS) onto the surface metal atoms was calculated. Here, two electronic properties based on d-PDOS of surface Ni atoms in Ni and Ni₃M alloy were analyzed. These are d-band center (ε_d) and local d-density of states (N_{E_F}) at Fermi level (E_F). The ε_d and N_{E_F} were considered for each Ni(111), Ni₃Fe(111) and Ni₃Cu(111) pristine surface to understand the changes in the electronic structure of Ni in the alloy surfaces with respect to Ni metal surface. The ε_d value defined within the framework of the Hammer-Norskov model of the surface Ni atoms in each surface structure was a measure of average energy of the unoccupied and occupied electronic states in the d-level of the metallic surface. These values were calculated and given in Table 4. The ε_d value of the surface Ni atoms in Ni(111) was calculated to be -1.28 eV, which was similar to the value reported in a previous studies [28]. With respect to Ni(111) the ε_d of surface Ni atoms in Ni₃Fe(111) shifted slightly downward with reference to E_F; whereas, in Ni₃Cu(111) the ε_d shifted significantly upward with reference to E_F. Such shifting away from E_F in Ni₃Fe(111) was also observed previously for Ni to Fe ratio greater than 1 [71]. The interatomic distance between Ni atoms in the top and second layer was measured to be 2.50 Å on Ni(111), 2.51 Å on Ni₃Fe(111) and 2.52 Å on Ni₃Cu(111). This suggests that strain effect induced by alloying on the electronic structure of Ni is minimal. Thus, the shift in ε_d is believed to be associated with the "ligand effect". The possibility of charge transfer from Fe to Ni in Ni₃Fe(111) surface cannot be ruled out as Ni and Fe have electronegativity of -1.91 and -1.83, respectively [71]. In contrast, the charge transfer from Cu to Ni would be negligible as their electronegativity values differ by 0.01 [72].

Another important electronic property is N_{E_F}, which is a measure of the number of electronic states that can be excited from occupied to unoccupied states at the lowest energy cost. Hence, N_{E_F} is indicative of the ability of the surface to respond to an external perturbation through a population of the unoccupied states [73]. An external perturbation may include the presence of a 'reactant' above the surface. The N_{E_F} values were also calculated for each surface and reported in Table 4. A large drop in N_{E_F} was observed while going from Ni(111) to Ni₃Fe(111). In contrast, a slight increase in N_{E_F} was observed in Ni₃Cu(111). Escano et al. reported that charge transfer and spin polarisation at E_F play a strong role in causing possible changes in N_{E_F} [73]. Fe is known to be much more magnetic in nature than Cu and, hence, large spin polarisation at E_F can occur. Furthermore, the difference in electronegativity with respect to Ni is higher for Fe than Cu. Thus, the observed changes in N_{E_F} due to charge transfer and spin polarisation at E_F can be well perceived.

The lower spin polarisation at E_F and negligible charge transfer characterizes the change in the electronic structure of Ni atoms in Ni₃Cu(111), which is reflected by significant change in ε_d and small change in N_{E_F}. Whereas, significant charge transfer and spin polarisation at E_F cause change to the Ni electronic structure in Ni₃Fe(111), which is reflected by slight change in ε_d and significant

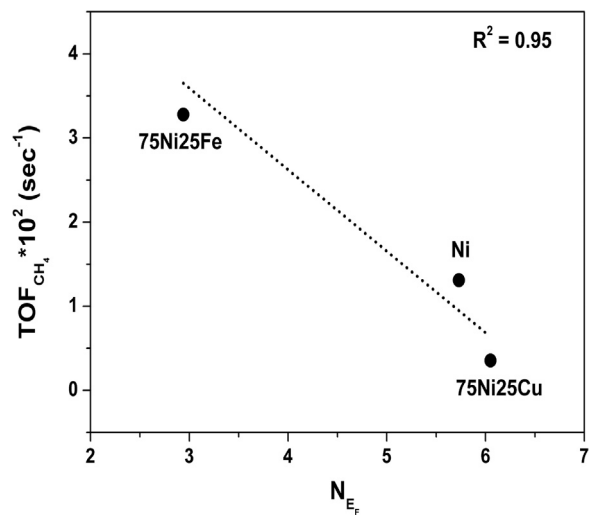


Fig. 6. Correlation between catalytic activity and electronic property of 15Ni/Al₂O₃ and 75Ni25M/Al₂O₃ catalysts. M = Cu or Fe. Reaction temperature T = 523 K.

change in N_{E_F}. These contrasting reasons bring about the changes in the electronic nature of Ni in the Ni-M alloy system and could have a significant effect on the surface reactivity of the supported catalysts.

Previous studies have also attempted to correlate the ε_d with reactivity parameters [2,28]. The ε_d value was found to be correlated with the catalytic activity of alloy catalysts for C=O hydrogenation to methane and the decomposition of oxygenates [2]. Apart from ε_d , there exists correlation between chemisorption energy of the adsorbate and d density of states at Fermi level [73,74]. In the present work the correlation between TOF_{CH₄} and ε_d was relatively poor. Instead, the correlation between TOF_{CH₄} and N_{E_F} was found to be much better, as shown in Fig. 6. The R² value (0.95) of the fitted straight line revealed an excellent fit between catalytic activity and surface electronic property. This justifies the suitability of using N_{E_F} as another important electronic descriptor. Furthermore, a previous study linearly correlated the surface electronic property with binding energies of the adsorbate [75]. The binding energy was then used to correlate with the hydrogenation activity of cyclohexane over Pt, Ni and Pt-Ni catalysts. The present work revealed that the surface electronic property N_{E_F} is linearly correlated with the TOF_{CH₄} and is an excellent descriptor to explain the catalytic activity of supported Ni, Ni-Cu and Ni-Fe catalysts. It is due to the increase in density of d electronic states of Ni metal at the Fermi level for the Ni-Cu alloy that the activity for CO₂ methanation is not favoured, whereas the lower number of d-states availability at the Fermi level for the Ni-Fe alloy favour CO₂ activation and subsequent methanation. The correlation between N_{E_F} and TOF_{CH₄} also helps us to understand why some Ni alloy catalysts are active and why some are not. Furthermore, it is an improved descriptor compared to surface ε_d for the CO₂ methanation reaction.

Thus, the present study reveals that Ni-M alloys (with the ratio of Ni to M as 3:1 and M = Fe or Cu) are formed for the supported Ni-based catalysts. However, formation of Ni-M alloys does not guarantee enhancement in catalytic activity. Only Ni-Fe alloy catalysts show enhanced activity relative to monometallic Ni for the CO₂ hydrogenation to CH₄ reaction, whereas Ni-Cu alloy does not. The changes in the activity parameter, TOF_{CH₄}, does not correlate with changes in surface area, percentage metal oxide reduction, number of surface metal sites, or metal particle size of the catalysts. The optimized lattice constants of monometallic Ni and two Ni-M alloy catalysts also do not capture any trend with the activity parameter. Instead, one of the electronic properties of pure Ni and Ni-M (with the ratio of Ni to M as 3:1 and M = Fe or Cu) shows trends

that correlate with the activity parameter. Specifically, the surface electronic property based on d-density of states of Ni is an excellent parameter that strongly correlates with the trends in catalytic activity. Such an analysis suggests that the activity of the supported alloy catalysts is very much dependent on their electronic structure.

4. Conclusions

The CO_2 methanation reaction was studied over supported Ni, Ni-M and M catalysts, where M was Cu or Fe, for a total metal loading of 15 wt.%. Characterization results obtained from TPR revealed the higher reducibility of copper oxide compared to iron oxide. The lower extent of iron oxides reduction resulted in an overall lower reducibility of Al_2O_3 supported Ni-Fe relative to Ni-Cu catalysts. However, the extent of reduction of $15\text{Ni}/\text{Al}_2\text{O}_3$ and two Ni-M/ Al_2O_3 catalysts containing Ni to M in the ratio of 3:1 were similar. The formation of Ni based alloys in the reduced supported Ni-M (Ni:M = 3:1) catalysts were suggested from experimental XRD data. The DFT calculated XRD pattern of these two simulated catalysts and pure Ni strongly support the experimental evidence of alloy formation. Furthermore, availability of surface sites in Ni-Fe/ Al_2O_3 was more than Ni-Cu/ Al_2O_3 catalysts. Among all the catalysts only one Ni-M/ Al_2O_3 (M = Fe, Ni:Fe = 3:1) catalyst had an activity that was superior to pure Ni. It appears that the alloy activity plays a pivotal role in producing a superior catalyst. In contrast, supported Ni-Cu alloy produced catalysts that had lower activity. The drop in activity for the supported Ni-Cu catalysts was due to formation of the relatively inactive Ni-Cu alloy and surface enrichment of the catalyst with inactive Cu metal. Deeper insights of the supported alloy catalysts were obtained thorough DFT calculations. The change in the electronic structure of Ni and Ni in the two alloy catalysts was non-monotonic due to the presence of Cu or Fe. The calculated electronic properties for pristine surfaces, (ε_d) and (N_{Ep}), assisted in the understanding of the catalytic phenomena. Charge transfer and spin polarisation mediated electronic property change for Ni in 75Ni25Fe alloy catalyst is a significant finding. Finally, it is one of the surface electronic properties, N_{Ep} , which provided the best correlation between surface properties of the catalysts and catalytic activity for the formation of CH_4 during CO_2 hydrogenation. The present study reveals that the local d-density of states at Fermi level of the pristine surface is the better descriptor for the catalytic activity of the Ni based alloy catalysts and pure Ni for the CO_2 hydrogenation reaction. Thus, another potential descriptor, other than ε_d , is proposed in this study that correlates well with the surface reactivity. Insights obtained from this study for the alloy catalysts and knowledge of the descriptor will further elucidate the mechanistic aspects and develop efficient catalysts for other products of the CO_2 hydrogenation reaction network.

Acknowledgements

The authors gratefully acknowledge the support from the Council of Scientific and Industrial Research (CSIR), Project No. 22(0634)/13/EMR-II. We would also like to acknowledge Mr. Rahul Bhardwaj, Advanced Imaging Centre, IIT Kanpur for assisting us with the TEM micrographs.

Appendix A. Supplementary data

Supplementary data associated with this article can be found, in the online version, at <http://dx.doi.org/10.1016/j.apcatb.2017.07.009>.

References

- [1] W. Wang, S. Wang, X. Ma, J. Gong, *Chem. Soc. Rev.* 40 (2011) 3703–3727.
- [2] M.D. Porosoff, J.G. Chen, *J. Catal.* 301 (2013) 30–37.
- [3] U. Rodemerck, M. Holena, E. Wagner, Q. Smejkal, A. Barkschat, M. Baerns, *ChemCatChem* 5 (2013) 1948–1955.
- [4] M.R. Gogate, R.J. Davis, *Catal. Commun.* 11 (2010) 901–906.
- [5] W. Wang, J. Gong, *Front. Chem. Sci. Eng.* 5 (2011) 2–10.
- [6] J.A. Rodriguez, J. Evans, L. Feria, A.B. Vidal, P. Liu, K. Nakamura, F. Illas, *J. Catal.* 307 (2013) 162–169.
- [7] M.A.A. Aziz, A.A. Jalil, S. Triwahyono, A. Ahmada, *Green Chem.* 17 (2015) 2647–2663.
- [8] J. Wambach, A. Baiker, A. Wokaun, *Phys. Chem. Chem. Phys.* 1 (1999) 5071–5080.
- [9] G.D. Weatherbee, C.H. Bartholomew, *J. Catal.* 77 (1982) 460–472.
- [10] F. Polymos, A. Erdohelyi, T. BANSAGI, *J. Catal.* 68 (1981) 371–382.
- [11] D. Pandey, G. Deo, *J. Mol. Catal. A: Chem.* 382 (2014) 23–30.
- [12] T. Das, G. Deo, *J. Mol. Catal. A: Chem.* 350 (2011) 75–82.
- [13] Y. Yan, Y. Dai, H. He, Y. Yu, Y. Yang, *Appl. Catal. B Environ.* 196 (2016) 108–116.
- [14] J. Polanski, T. Siudyga, P. Bartczak, M. Kapkowski, W. Ambrozkiewicz, A. Nobis, R. Sitko, J. Klimontko, J. Szade, J. Lelatko, *Appl. Catal. B Environ.* 206 (2017) 16–23.
- [15] C. Swalus, M. Jacquemin, C. Poleunis, P. Bertrand, P. Ruiz, *Appl. Catal. B Environ.* 125 (2012) 41–50.
- [16] G. Garbarino, D. Bellotti, P. Riani, L. Magistri, G. Busca, *Int. J. Hydrogen Energy* 40 (2015) 9171–9182.
- [17] M.A.A. Aziz, A.A. Jalil, S. Triwahyono, R.R. Mukti, Y.H. Taufiq-Yap, M.R. Sazegar, *Appl. Catal. B Environ.* 147 (2014).
- [18] C. Jia, J. Gao, J. Li, F. Gu, G. Xu, Z. Zhong, F. Su, *Catal. Sci. Technol.* 3 (2013) 490–499.
- [19] A.L. Kustov, A.M. Frey, K.E. Larsen, T. Johannessen, J.K. Nørskov, C.H. Christensen, *Appl. Catal. A: Gen.* 320 (2007) 98–104.
- [20] B. Mutz, H.W.P. Carvalho, S. Mangold, W. Kleist, J.-D. Grunwaldt, *J. Catal.* 327 (2015) 48–53.
- [21] G. Garbarino, P. Riani, L. Magistri, G. Busca, *Int. J. Hydrogen Energy* 39 (2014) 11557–11565.
- [22] A.E. Aksyolyu, A.N. Akin, Z.I. Onsan, D.L. Trimm, *Appl. Catal. A: Gen.* 145 (1996) 185–193.
- [23] J. Sehested, K.E. Larsen, A.L. Kustov, A.M. Frey, T. Johannessen, T. Bligaard, M.P. Andersson, J.K. Nørskov, C.H. Christensen, *Top. Catal.* 45 (2007) 9–13.
- [24] D. Pandey, G. Deo, *J. Ind. Eng. Chem.* 33 (2016) 99–107.
- [25] Q. Wu, W.L. Eriksen, L.D.L. Duchstein, J.M. Christensen, C.D. Damsgaard, J.B. Wagner, B. Temel, J.-D. Grunwaldt, A.D. Jensen, *Catal. Sci. Technol.* 4 (2014) 378–386.
- [26] Q. Wu, L.D.L. Duchstein, G.L. Chiarello, J.M. Christensen, C.D. Damsgaard, C.F. Elkjaer, J.B. Wagner, B. Temel, J.-D. Grunwaldt, A.D. Jensen, *ChemCatChem* 6 (2014) 301–310.
- [27] B. Hammer, J.K. Nørskov, *Surf. Sci.* 343 (1995) 211–220.
- [28] B. Hammer, J.K. Nørskov, *Adv. Catal.* 45 (2000) 71–129.
- [29] J.K. Nørskov, T. Bligaard, B. Hvolbaek, F. Abild-Pedersen, I. Chorkendorff, C.H. Christensen, *Chem. Soc. Rev.* 37 (2008) 2163–2171.
- [30] J.K. Nørskov, F. Abild-Pedersen, F. Studd, T. Bligaard, *PNAS* 108 (2011) 937–943.
- [31] A. Vojdovic, J.K. Nørskov, F. Abild-Pedersen, *Top. Catal.* 57 (2014) 25–32.
- [32] W. Yu, M.A. Barteau, J.G. Chen, *J. Am. Chem. Soc.* 133 (2011) 20528–20535.
- [33] M. Tamura, K. Kon, A. Satsuma, K.-i. Shimizu, *ACS Catal.* 2 (2012) 1904–1909.
- [34] S. Furukawa, K. Ehara, K. Ozawa, T. Komatsu, *Phys. Chem. Chem. Phys.* 16 (2014) 19828–19831.
- [35] H. Abe, H. Yoshikawa, N. Umezawa, Y. Xu, G. Saravanan, G.V. Ramesh, T. Tanabe, R. Kodiyath, S. Ueda, N. Sekido, Y. Yamabe-Mitarai, M. Shimoda, T. Ohno, F. Matsumoto, T. Komatsu, *Phys. Chem. Chem. Phys.* 17 (2015) 4879–4887.
- [36] S. Sengupta, K. Ray, G. Deo, *Int. J. Hydrogen Energy* 39 (2014) 11462–11472.
- [37] S.B. Simonsen, D. Chakraborty, I. Chorkendorff, S. Dahl, *Appl. Catal. A: Gen.* 447–448 (2012) 22–31.
- [38] S.J. Clark, M.D. Segall, C.J. Pickard, P.J. Hasnip, M.I.J. Probert, K. Refson, M.C. Payne, *Z. Kristallogr.* 220 (2005) 567–570.
- [39] J.P. Perdew, K. Burke, Y. Wang, *Phys. Rev. B* 54 (1996) 16533–16539.
- [40] J.P. Perdew, K. Burke, M. Ernzerhof, *Phys. Rev. Lett.* 77 (1996) 3865–3868.
- [41] H.J. Monkhorst, J.D. Pack, *Phys. Rev. B* 13 (1976) 5188–5192.
- [42] M.-S. Fan, A.Z. Abdullah, S. Bhatia, *Appl. Catal. B Environ.* 100 (2010) 365–377.
- [43] M. Rao, S. Sturm, F. Philipp, M.V. Zinkevich, *Int. J. Mater. Res.* 97 (2006) 789–793.
- [44] J. BULARZIK, P.K. DAVIES, A. NAVROTSKY, *J. Am. Ceram. Soc.* 69 (1986) 453–457.
- [45] A.E. Bianchi, L. Montenegro, R. Vina, G. Punte, *Powder Diffr.* 23 (2008) S81–S86.
- [46] L.D. Rogatis, T. Montini, A. Cognigni, L. Olivi, P. Fornasiero, *Catal. Today* 145 (2009) 176–185.
- [47] P. Schouwink, L.S. Dubrovinsky, K.V. Glazyrin, M. Merlini, M. Hanfland, T. Pippinger, R. Miletich, *Am. Miner.* 96 (2011) 1781–1786.
- [48] E. Solano, C. Frontera, T. Puig, X. Obradors, S. Ricart, J. Ros, *J. Appl. Cryst.* 47 (2014) 414–420.
- [49] R. Brown, M.E. Cooper, D.A. Whan, *Appl. Catal. A* 3 (1982) 177–186.
- [50] L. Zhang, Xueqin Wang, B. Tan, U.S. Ozkan, *J. Mol. Catal. A: Chem.* 297 (2009) 26–34.
- [51] S.D. Robertson, B.D. Mcnicol, J.H.D. Baas, S.C. Kloet, *J. Catal.* 37 (1975) 424–431.
- [52] Q. Guo, M. Wu, K. Wang, L. Zhang, X. Xu, *Ind. Eng. Chem. Res.* 54 (2015) 890–899.
- [53] S. Sitthisa, W. An, D.E. Resasco, *J. Catal.* 284 (2011) 90–101.

[54] S. Logdberg, D. Tristantini, Ø. Borg, L. Ilver, B. Gevert, S. Jaras, E.A. Blekkan, A. Holmen, *Appl. Catal. B Environ.* 89 (2009) 167–182.

[55] M.M. Yung, E.M. Holmgreen, U.S. Ozkan, *J. Catal.* 247 (2007) 356–367.

[56] S.A. Khromova, A.A. Smirnov, O.A. Bulavchenko, A.A. Saraev, V.V. Kaichev, S.I. Reshetnikov, V.A. Yakovlev, *Appl. Catal. A: Gen.* 470 (2014) 261–270.

[57] R.P. van Ingen, R.H.J. Fastenau, E.J. Mittemeijer, *J. Appl. Phys.* 76 (1994) 1871–1883.

[58] S. Ochiai, Y. Mishima, T. Suzuki, *Bull. Res. Lab. Precis. Mach. Electron. (Tokyo Inst Technol)* 53 (1984) 15–28.

[59] S.L. Pirard, J.G. Mahy, J.-P. Pirard, B. Heinrichs, L. Raskinet, S.D. Lambert, *Microporous Mesoporous Mater.* 209 (2015) 197–207.

[60] C.R. Brundle, E. Silverman, R.J. Madix, *J. Vac. Sci. Technol.* 16 (1979) 474–477.

[61] V. Ponec, G.C. Bond, *Catalysis by Metals and Alloys*, Elsevier, Amsterdam, 1995.

[62] M.G. Prakash, R. Mahalakshmy, K.R. Krishnamurthy, B. Viswanathan, *Catal. Today* 263 (2016) 105–111.

[63] T. Ishihara, K. Eguchi, H. Arai, *Appl. Catal.* 30 (1987) 225–238.

[64] G.D. Weatherbee, C.H. Bartholomew, *J. Catal.* 87 (1984) 352–362.

[65] H. Wei, K. Xie, J. Zhang, Y. Zhang, Y. Wang, Y. Qin, J. Cui, J. Yan, Y. Wu, *Sci. Rep.* 4 (2014).

[66] Y. Liu, D. Liu, *Int. J. Hydrogen Energy* 24 (1999) 351–354.

[67] M. Winiarski, P. Scharoch, *Comput. Mater. Sci.* 48 (2010) 700–704.

[68] W. An, X.C. Zeng, C.H. Turner, *J. Chem. Phys.* 131 (2009) 174702–174711.

[69] Y. Mishin, M.J. Mehl, D.A. Papaconstantopoulos, *Acta Mater.* 53 (2005) 4029–4041.

[70] G. Bozzolo, J. Ferrante, *NASA Tech. Pap.* 3155 (1991).

[71] C. Fan, X.-G. Zhou, D. Chen, H.-Y. Cheng, Y.-A. Zhu, *J. Chem. Phys.* 134 (2011) 134704–134715.

[72] H.H. Hsieh, Y.K. Chang, W.F. Pong, J.Y. Pieh, P.K. Tseng, *Phys. Rev. B* 57 (2001) 15204–15207.

[73] M.C. Escano, T.Q. Nguyen, H. Nakanishi, H. Kasai, *J. Phys.: Condens. Matter* 21 (2009) 492201–492206.

[74] M.P. Hyman, B.T. Loveless, J.W. Medlin, *Surf. Sci.* 601 (2007) 5382–5393.

[75] M.D. Porosoff, W. Yu, J.G. Chen, *J. Catal.* 308 (2013) 2–10.